A high-performance interface for grounded conductivity sensors

Xiujun Li and Gerard C M Meijer

Faculty of Information Technology and Systems, Delft University of Technology, Mekelweg 4,
2628 CD Delft, The Netherlands

E-mail: X.Li@tudelft.nl

Abstract
This paper presents a high-performance interface for grounded conductivity sensors. The
interface mainly consists of a sensor driver, an analog front-end, a multiplexer and a
voltage-to-time converter. The sensor driver and analog front-end provide a controlled
excitation voltage for the sensor and convert the sensor signal (conductance) into a voltage
signal. The voltage-to-time converter acts as an asynchronous converter that employs a
relaxation oscillator to convert the sensor signals (voltages) into a period-modulated output
voltage. The analysis and experiments are performed to optimize the interface circuit with
respect to the range of measurable conductance. With a prototype, over a wide conductance
range, from 0.01 μS to 1 mS, the experimental results show random errors with a standard
deviation of less than 5.6 nS for a measurement time of 160 ms, and a systematic error of less
than 22 nS.

Keywords: sensor interface, oscillators, grounded conductance measurement

1. Introduction

Conductivity sensors are used in various measurement and
control systems, for instance, in applications for measuring
the properties of biological and chemical materials, for
monitoring the environment, for control purposes in chemical
processes and for agriculture and food production [1–5].
Thus, performing an accurate and reliable measurement of the
conductance is very important for applying the conductivity
sensors. In some applications, the system allows the
conductivity sensor to be galvanically floating with respect
to the interface circuit. In this case, the interface designer
is free to connect the sensor that does not disturb biasing
of the interface. However, due to safety reasons and/or
operating limitations of floating conductivity sensors, in some
applications conductivity sensors have to be grounded [6, 7].
When the sensors are in galvanic contact with a conductive
liquid, polarization and electro-chemical effects can easily
cause electrode corrosion. In order to reduce these effects,
the fact that the excitation signal contains a dc component
should be avoided.

An important feature of the conductance measurement
is its dynamic measurement range. Generally, the range
of measured conductivity is very wide, for instance, from

0.05 μS cm^{-1} for pure water to 55 mS cm^{-1} for ocean water.
By selecting conductivity sensors with different cell constants,
the measurement range of the conductance can be optimized.
For our design, a conductance measurement range of 0.5 μS
to 10 mS has been targeted, which could cover a broad range
of applications. Regarding the resolution, our design target is
0.05 μS.

This paper presents the design of a low-cost and accurate
interface for grounded conductivity sensors. In this interface,
many advanced techniques are applied, such as the chopping
technique that reduces the dc offset and low-frequency noise
of the electronics, and the auto-calibration technique that
ensures high reliability of the measurement system. The
interface is optimized with respect to the range of measurable
conductance.

The proposed interface is suitable to be applied for both
two-electrode and four-electrode conductivity sensors.

2. The interface system

2.1. Basic principles of conductivity sensor and measurement

Generally, the conductivity sensor is equipped with four or
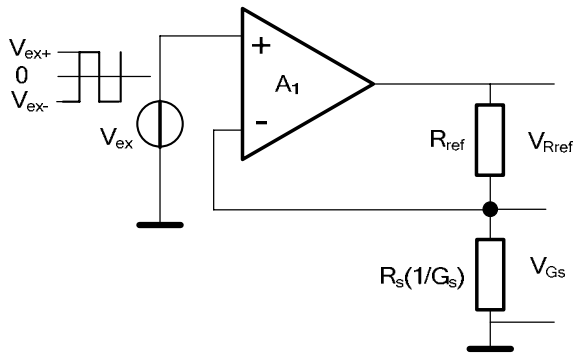two electrodes. The four-electrode conductivity sensor, which

Figure 1. The basic principle of the driving circuit for the measurement of the grounded conductivity sensors.

reduces the effect of the connection wires, is mainly used to measure high conductance values. For lower conductance values the simpler two-electrode sensor can be used. For actual conductivity sensors, its measurement is affected by many non-idealities, including contact potentials, contact impedances and temperature drift. The magnitudes of these effects depend on the materials of the electrode and the object. Generally, they are not stable. Therefore, for an accurate and reliable measurement, the influence of these parasitics should be eliminated or significantly reduced.

The effects of dc contact potentials on the measurement of a conductance G_S can be eliminated by using an ac excitation signal for the sensor. To eliminate the effect of the contact impedances as well as the effect of the lead-wire resistance, a four-wire measurement is applied.

As shown in [8, 9], a floating conductance G_S can be measured using an ac voltage excitation V_{ex}. In contrast to this, the circuit presented in this paper should be designed for the measurement of grounded conductances. The driving circuit (figure 1) has been designed just for this application. In this circuit, by the feedback loop around the amplifier A_1, the voltage V_{Gs} over the conductance is fixed to the value of V_{ex}. In the case of ideal amplifiers that have a very high loop gain, a negligible input current and an offset voltage, the voltage V_{Gs} over the conductance G_S equals V_{ex}. The current flow

I_{Gs} equals the current through R_{ref}. Therefore, the measured conductance equals

$$G_S = \frac{I_{Gs}}{V_{Gs}} = \frac{V_{Rref}}{V_{ex}} \frac{1}{R_{ref}}. \tag{1}$$

Equation (1) shows that from the measured values of the voltages V_{ex} and V_{Rref} the conductance can be calculated.

2.2. A circuit diagram of the interface

Figure 2 shows a simplified schematic diagram of the proposed interface, which mainly consists of a sensor driver, an analog front-end, a multiplexer and a voltage-to-time converter.

As shown in the above section, the amplifier AMP1 is employed to establish a controlled excitation voltage V_{Gs} across the measured conductance G_S. The voltage V_{Gs} is equal to the voltage V_{ex}. To avoid electrolysis, this voltage should be bipolar and its dc component less than the free corrosion potential. The current flow I_{Gs}, which is equal to the current through the resistor R_{ref}, is measured by measuring the voltage V_{Rref} across the resistor R_{ref}. Both voltages V_{ex} and V_{Rref} are sequentially measured using the voltage-to-time converter.

The voltage-to-time converter linearly converts the sensor signal (voltage) and the reference signal (voltage) into period-modulated signals by employing a relaxation oscillator. The relaxation oscillator is implemented with an amplifier (AMP2), a comparator (COMP), two inverters (IV), two capacitors (C_{off} and C_{int}) and a resistor R_{int}. The details of this relaxation oscillator and its performance have been described in [11, 12]. The capacitor C_s is used to convert the output voltage of the AMP1 into the charge. The multiplexer MUX (figure 2) selects the signal to be measured, V_{ex}, V_{Rref}, $V_{off,Rref}$ or $V_{off,Gx}$, where $V_{off,Rref}$ and $V_{off,Gx}$ are the offset measurements at the corresponding CM voltage levels. The capacitor C_s samples one of these four voltage signals.

With the relaxation oscillator, an ac square-wave excitation signal V_{ex} is generated. The use of ac signals is important to reduce the electro-chemical effects and the effects of dc drift and parasitic Seebeck voltages. Meanwhile, the ac square-wave excitation signal is also used to implement
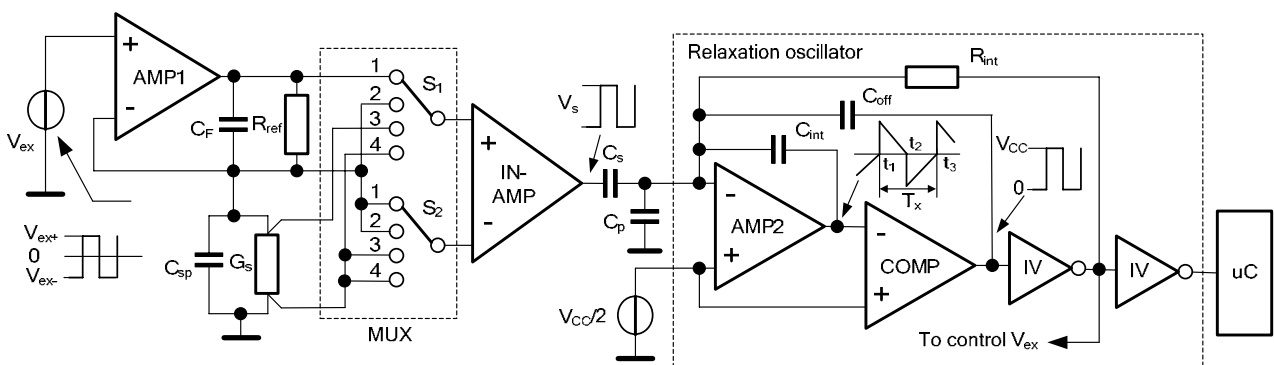

Figure 2. A simplified interface for the grounded conductance measurement.

the chopping technique [9, 10], synchronized with voltage-to-time conversion. The chopping technique is implemented in the following way: when V_{ex} makes an up-going step, a positive charge $V_s C_s$ is converted into a time interval and when V_{ex} makes a down-going step, a negative charge $-V_s C_s$ is converted into a time interval. The sum of these two time intervals composes a period of the oscillator signal. The chopping technique reduces the effects of offset, $1/f$ noise and low-frequency interference, significantly. This enables the use of low-cost CMOS technology for accurate measurement systems.

The offset capacitor C_{off} is used to bring the oscillator frequency within its linear range. The capacitor C_p represents the parasitic capacitance including the connection-wire's and component's capacitances. This capacitance will affect the noise performance of the interface (see section 3).

As presented in [11, 12], the period of the relaxation oscillator equals

$$T = 4R_{int} \frac{V_s C_s + V_{CC} C_{off}}{V_{CC}} + \tau = 4R_{int} C_s \frac{V_s}{V_{CC}} + 4R_{int} C_{off} + \tau,$$

(2)

where τ is the delay time of the oscillating loop. From this relation, it can be found that once R_{int} is defined C_{off} will determine the maximum frequency of the oscillator and that C_s will determine the dynamic range of the oscillator.

During the measurement phases of V_{ex}, V_{Rref}, $V_{off,ref}$ and $V_{off,Gs}$, the period times of the output signal of the oscillator amount to T_{VGs}, T_{IGs}, $T_{off,Gs}$ and $T_{off,ref}$, respectively. These period times amount to

$$T_{VGs} = 4R_{int} C_s \frac{V_{ex}}{V_{CC}} + (4R_{int} C_{off} + \tau_1)$$

$$T_{IGs} = 4R_{int} C_s \frac{V_{Rref}}{V_{CC}} + (4R_{int} C_{off} + \tau_2)$$

(3)

$$T_{off,Gs} = 4R_{int} C_{off} + \tau_1$$

$$T_{off,ref} = 4R_{int} C_{off} + \tau_2,$$

where τ_1 and τ_2 represent the additive errors including those which depend on the common-mode voltage. From equations (1)–(3), for the conductance G_S it can be found that

$$G_S = \frac{T_{IGs} - T_{off,ref}}{T_{VGs} - T_{off,Gs}} \cdot \frac{1}{R_{ref}}.$$

(4)

This result does not depend on the unknown parameters of the interface, R_{int}, V_{CC}, C_s, C_{off}, τ_1 and τ_2. In this way, the interface is auto-calibrated for additive or multiplicative errors. Even in the case of slow variations of all these parameters, their effects are eliminated. Also, the effects of the input offset voltage and biasing current of amplifiers are eliminated. The algorithm can be implemented using, for instance, a microcontroller.

3. Non-idealities

As described in section 2, many unknown parameters of the interface are eliminated by means of auto-calibration (equation (4)). Also, the use of this auto-calibration will eliminate the effects of many non-idealities of the amplifier

(AMP2) and comparator (COMP). For instance, the input offset voltages of the amplifier and comparator will induce an offset error on the oscillator period. The biasing current of the amplifier and the asymmetry of the comparator output with respect to $V_{CC}/2$ will induce a multiplicative error in the oscillator period. These multiplicative and offset errors will be eliminated by the use of auto-calibration. However, some effects cannot be eliminated by this technique and should be taken into account during the interface design.

3.1. Noise

For the conductance measurement with the interface shown in figure 2, the noise originates mainly from three parts: the oscillator thermal noise, amplifier noise (AMP1 and IN-AMP) and the quantization noise caused by sampling in the microcontroller. As compared to the amplifier noise, the thermal noise of the reference resistor (in our case $R_{ref} < 1$ kΩ) is negligible. Now, the relative errors caused by these three noise sources will be analyzed.

3.1.1. Oscillator thermal noise. As described in [11, 13], the oscillator thermal noise is mainly determined by the noise properties of the integrator amplifier and comparator. When the comparator is implemented with an opamp with a limited bandwidth, then its noise contribution can be neglected. The oscillator noise is mainly due to the noise of the amplifier AMP2 (figure 2) and is affected by the integrator bandwidth and the measurement time. As discussed in [11, 13], the normalized noise error of the oscillator is defined as

$$\zeta = \frac{\Delta T_x}{T_x} = \frac{t_{n1} + t_{n2}}{T_x}$$

$$= \frac{C_{int}}{2(V_{CC} C_{off} + V_s C_s)} (2\upsilon_n(t_2) - \upsilon_n(t_1) - \upsilon_n(t_3)),$$

(5)

where $\upsilon_n(t_1)$, $\upsilon_n(t_2)$ and $\upsilon_n(t_2)$ are the noise voltages at the input of the comparator at the switching moments t_1, t_2 and t_3 (indicated in figure 2), respectively. The standard deviation σ_{nosc} of (5) is given by

$$\sigma_{nosc} = \sqrt{\int_0^{B_{eq}} |H_v(jf)|^2 S_v(f) \, df},$$

(6)

where $S_v(f)$ is the power spectral density (PSD) of the input noise υ_n and B_{eq} is the equivalent bandwidth of the system. For one sinusoidal component of the input noise, in the frequency domain the transfer function $|H_v(jf)|$ is given by [11]

$$|H_v(jf)| = \frac{2C_{int}}{(V_{CC} C_{off} + V_s C_s)} \sin^2\left(\frac{\pi f}{2} T_x\right).$$

(7)

For the input noise voltage υ_{amp2} of the AMP2, its equivalent PSD at the input of the comparator is given by [11]

$$S_v(f) = S_{v amp2}(f) \left(\frac{C_{off} + C_s + C_{int} + C_p}{C_{int}}\right)^2,$$

(8)

where $S_{v amp2}$ is the power spectral density (PSD) of the input noise υ_{amp2} of the AMP2 and C_p is the parasitic capacitance from the inverting input of AMP2 to the ground.

In our case, the bandwidth B_{eq} is limited by the bandwidth f_T of amplifier AMP2, which is

$$B_{eq} = B_{amp2} = \left(\frac{C_{int}}{C_{off} + C_s + C_{int} + C_p} \right) f_T. \quad (9)$$

From equations (6)–(9), for a single period of the oscillator output, the standard deviation of the oscillator noise σ_{nosc} is found to be

$$\sigma_{nosc,single} = \frac{C_{int}}{V_{CC}C_{off} + V_s C_s}$$
$$\times \sqrt{\frac{3}{2} \frac{(C_{off} + C_s + C_{int} + C_p)}{C_{int}} f_T S_{vamp2}}. \quad (10)$$

For $N \, (N \gg 1)$ periods of the oscillator output, the standard deviation of the oscillator noise σ_{nosc} equals

$$\sigma_{nosc,N} = \frac{\sigma_{nosc,\,single}}{\sqrt{N}}. \quad (11)$$

So, the standard deviation of the oscillator noise is reduced with the square root of the number of periods (N).

3.1.2. Amplifier noise (AMP1 and IN–AMP). With figure 1 and equation (1), it can be calculated that the noise σ_{namp1} caused by the noise of the amplifier AMP1 amounts to

$$\sigma_{namp1} \approx \sqrt{\frac{v_{amp1}^2}{V_{ex}^2}\left(1 + \frac{V_{ref}^2}{V_{ex}^2}\right)} = \sqrt{\frac{v_{amp1}^2}{V_{ex}^2}\left(1 + R_{ref}^2 G_S^2\right)}, \quad (12)$$

where v_{amp1} is the RMS value of the equivalent input noise of AMP1.

A similar result is found for the effect of the noise of amplifier IN–AMP, which has unity gain. When considering a measurement over N periods, the total-noise contribution of both amplifiers, AMP1 and IN–AMP, is given by

$$\sigma_{namp} \approx \sqrt{\frac{v_{amp1}^2 + v_{INamp}^2}{N V_{ex}^2}\left(1 + R_{ref}^2 G_S^2\right)}, \quad (13)$$

where v_{INamp} denotes the RMS values of the equivalent input noise of the IN–AMP.

3.1.3. Quantization noise. Digitizing the period times with a counter will cause quantization noise. The level of this quantization noise depends on the length of the period time and the counter clock. As described in [11, 13], the standard deviation of the relative error σ_{nqt} caused by the quantization noise amounts to

$$\sigma_{nqt} \approx \frac{1}{\sqrt{3}} \frac{1}{N T_p f_c}, \quad (14)$$

where f_c is the sampling frequency of the counter and T_p is the period time of the oscillator. The quantization noise is inversely proportional to the measurement time (NT_p). Equations (11)–(14) show that with increasing N, the quantization noise decreases more rapidly than the other two noise effects.
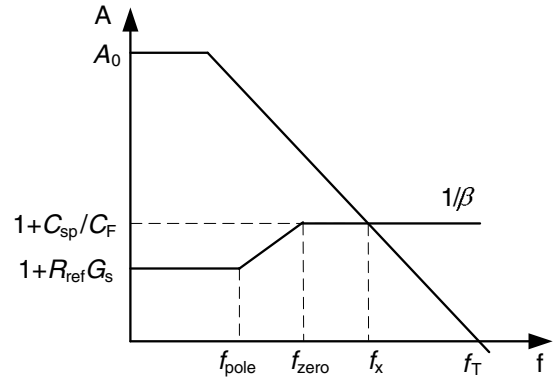

Figure 3. Magnitude Bode plot.

3.2. The leakage current of the multiplexer

The leakage current of the multiplexer will induce an additive error on the measured conductance. Only the leakage currents of the switches that are connected to the junction between R_{ref} and G_S contribute to the measurement error. The leakage currents $I_{Si,j}$ of the four multiplexer switches cause an error δG_S in the measurement of G_S, which amounts to

$$\delta G_S \approx -\frac{I_{S1,2} + I_{S1,3} + I_{S2,1} + I_{S2,2}}{V_{ex}}. \quad (15)$$

To reduce this error, a multiplexer with a low leakage current should be used.

3.3. Parasitic capacitance of the sensor

Due to the connecting cables, sensor structure and the interface circuit, there exists a parasitic capacitance C_{sp}, which is in parallel with the sensor. This parasitic capacitor will induce a zero in the transfer function of the sensor driver electronics, which will result in the stability problem.

To compensate for this effect, a feedback capacitor C_F is applied in parallel with R_{ref} (see figure 2). Figure 3 depicts the Bode plot for gain A and $1/\beta$ of the amplifier AMP1 in figure 2. From figure 2, the feedback factor β is found to be

$$\beta = \frac{1 + sR_{ref}C_F}{1 + R_{ref}G_S + sR_{ref}(C_F + C_{sp})}. \quad (16)$$

In this figure, f_T represents the unity-gain bandwidth of AMP1. Furthermore, the frequency values indicated along the horizontal axis are

$$f_{pole} = \frac{1 + R_{ref}G_S}{2\pi R_{ref}(C_F + C_{sp})}$$
$$f_{zero} = \frac{1}{2\pi R_{ref}C_F} \quad (17)$$
$$f_x = \frac{f_T}{1 + C_{sp}/C_F}.$$

To have a stable sensor driver, the following conditions should be met:

$$f_{pole} < f_x \qquad f_{zero} < f_x. \quad (18)$$

Then, from equations (17) and (18) the feedback capacitor C_F should be selected according to the condition

$$C_F > \max\left(\frac{1 + \sqrt{1 + 8\pi R_{\text{ref}} C_{\text{sp}} f_T}}{4\pi R_{\text{ref}} f_T}, \frac{1 + R_{\text{ref}} G_S}{2\pi R_{\text{ref}} f_T}\right). \quad (19)$$

It is shown that a large value of capacitor C_F makes AMP1 more stable. However, a large value of capacitor C_F will also induce a large error in the G_S measurement.

Suppose that the used amplifier (AMP1) has a unity-gain bandwidth $f_T \gg f_{\text{zero}}$ (see equation (17)), as defined in (1); in the frequency domain the measured conductance $G_{\text{sm}}(f)$ is given by

$$G_{\text{sm}}(f) = G_S \frac{1 + sC_{\text{sp}}/G_S}{1 + sR_{\text{ref}} C_F}. \quad (20)$$

Then, in the time domain the following result is obtained:

$$G_{\text{sm}}(t) \approx G_S + \frac{1}{R_{\text{ref}}}\left(\frac{C_{\text{sp}}}{C_F} - R_{\text{ref}} G_S\right) e^{-\frac{T_{IGs}}{2R_{\text{ref}} C_F}}. \quad (21)$$

So the error δG_S in the G_S measurement induced by the capacitor C_F amounts to

$$\delta G_S = G_{\text{sm}} - G_S = \frac{1}{R_{\text{ref}}}\left(\frac{C_{\text{sp}}}{C_F} - R_{\text{ref}} G_S\right) e^{-\frac{T_{IGs}}{2R_{\text{ref}} C_F}}. \quad (22)$$

3.4. Temperature drift

As described in section 2, the offset and gain errors of the interface are eliminated by applying auto-calibration (see also equation (4)). Auto-calibration will also eliminate the effects of changes caused by the drift of the offset voltage and interface gain as caused by temperature variations. Yet, the reference resistor R_{ref} should have a low-temperature coefficient because its temperature performance will directly affect the absolute measurement result of the conductance G_S (see equation (4)).

4. Range of measurable conductance

4.1. The minimum measurable conductance

The minimum measurable conductance (the resolution) is mainly limited by the noise level of the interface σ_{nG} and the choice of the reference resistor R_{ref}. The noise of the interface σ_{nG} is mainly composed of the three items mentioned in section 3. Then, the minimum measurable conductance $G_{x,\text{min}}$ is given by

$$G_{x,\text{min}} \geqslant \frac{\sigma_{nG}}{R_{\text{ref}}}, \quad (23)$$

which shows that a larger value of R_{ref} results in a better resolution.

4.2. The maximum measurable conductance

The maximum measurable conductance is mainly limited by the output drive current $I_{\text{OUT,max}}$ of the amplifier AMP1 and the linear dynamic range of the relaxation oscillator. With respect to $I_{\text{OUT,max}}$, the maximum measurable conductance $G_{x,\text{max}}$ is limited to $G_{x,\text{max}} \leqslant (I_{\text{OUT,max}}/V_{\text{ex}})$.

By reducing the amplitude of the excitation signal, the maximum measurable conductance can be increased.

However, this will increase the contribution of the amplifier noise (AMP1 and IN-AMP) too.

Concerning the linear dynamic range of the relaxation oscillator, the maximum voltage over reference resistor is designed as $V_{\text{Rref,max}} = R_{\text{ref}} I_{\text{OUT,max}} = V_{\text{ex}}$. So that, the maximum measurable conductance $G_{x,\text{max}}$ is given by

$$G_{x,\text{max}} \leqslant 1/R_{\text{ref}}.$$

In our design, the maximum measurable conductance $G_{x,\text{max}}$ is limited to $1/R_{\text{ref}}$.

5. Experimental results

The described conductivity-sensor interface has been implemented and tested, using the circuit shown in figure 2. For the operational amplifiers, dual OPAMPs (OPA2132PA) have been used. The relaxation oscillator is built with an amplifier (OPA2350), an inverter (HC04), a comparator implemented with an opamp (OPA2132PA) and some passive components. The circuit is powered by a dual power supply of ± 5 V. The multiplexer (MAX4559) has been chosen because of its low leakage current. The ac square-wave excitation signal is generated by the oscillator itself. To have the best performance, the values of passive components of the oscillator are selected as $R_{\text{int}} = 2$ MΩ, $C_{\text{off}} = 6.2$ pF, $C_{\text{s}} = 82$ pF and $C_{\text{int}} = 27$ pF. In this case, the frequency of the excitation signal amounts to 8–20 kHz depending on the value of the measured conductance. A fast microcontroller of the type LPC2101, which has a 70 MHz counting frequency, is employed to measure the output period of the oscillator. It also processes the data and communicates with the outside digital world. Because the performances of the reference resistor directly affect the measurement results, a high-precision type (tolerance: $< \pm 0.01\%$ and temperature coefficient: < 0.6 ppm $^\circ$C^{-1}) has been chosen. The performance of the interface has been tested for the case that the controlled excitation voltage V_{ex} has a peak-to-peak value of ± 200 mV. Depending on the electro-chemical properties, the amplitude of the excitation signal can be adjusted for a value less than the free corroding potential.

5.1. Standard deviation of the noise

The standard deviation of the interface was measured with $R_{\text{ref}} = 1000.06$ Ω and $G_S = 49.986$ μS, and was calculated with 500 measurement samples. The measurement standard deviation has also been determined as a function of the measurement time, which is the total time for the measurement of T_{VGs}, T_{IGs}, $T_{\text{off,Gs}}$ and $T_{\text{off,ref}}$. This measurement result is depicted in figure 4. As an example, for a measurement time of 160 ms, the measured standard deviation amounts to 5.6 nS for the range of 0.01 μS to 1 mS.

For very short measurement times, the quantization noise, which originates from the sampling by the microcontroller, is dominant. For these short times, the resolution is inversely proportional to the measurement time. For longer measurement time, the interface thermal noise is dominant, which is inversely proportional to the square root of the
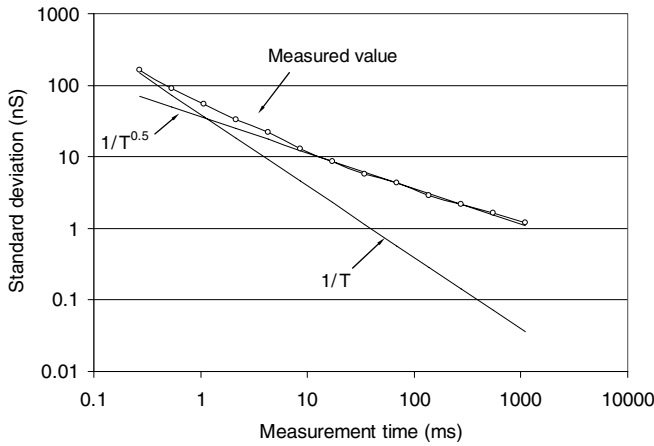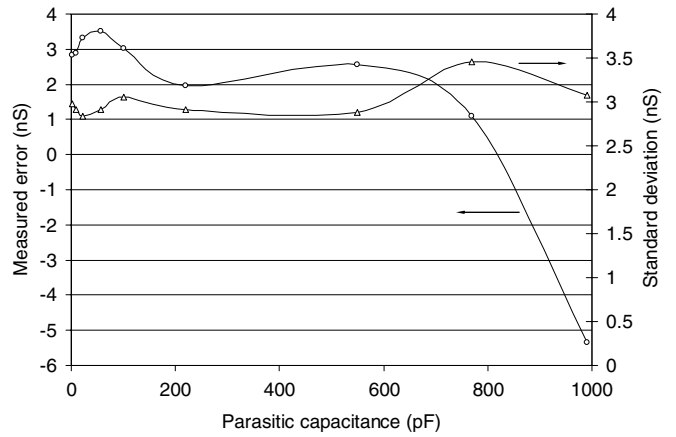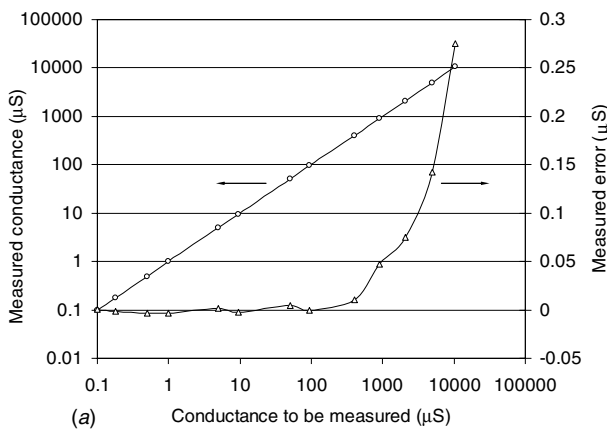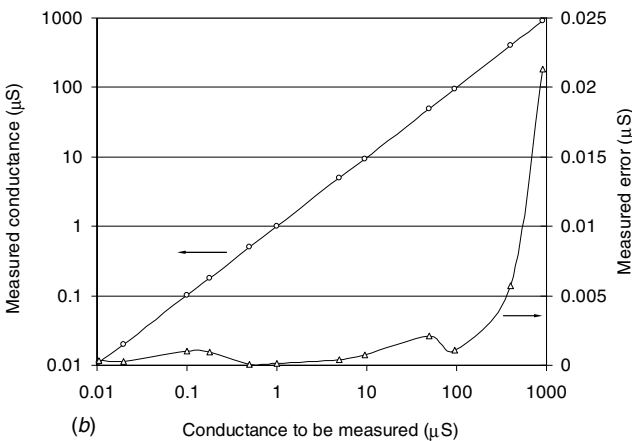
Figure 4. The measured standard deviation.

(*a*)

(*b*)

Figure 5. Systematic errors with (*a*) $R_{ref} = 104.065 \ \Omega$ and (*b*) $R_{ref} = 1000.06 \ \Omega$.

measurement time. A longer measurement time results in a lower noise level, therefore a smaller measurable conductance.

5.2. The systematic error

The systematic error of the interface was measured with a measurement time of 160 ms and two different reference-resistance values (104.065 Ω and 1000.06 Ω). The measurement results for the conductance G_s are depicted in figure 5.

Figure 6. The effect of the parasitic capacitance C_{sp} for the systematic error and the standard deviation.
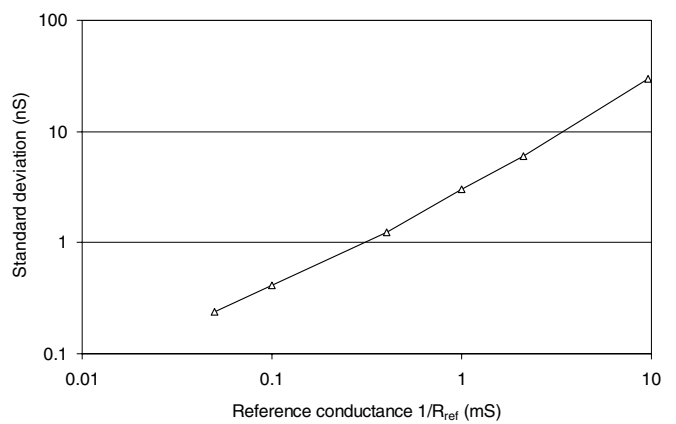

Figure 7. The effect of the reference resistor.

It is shown that the minimum measurable range is enlarged by increasing the value of R_{ref}. For high values of the conductance, as depicted at the right-hand side of the graph, the measured error increases linearly with the measured conductance. It should be noted that it concerns a linear error, which has been depicted on a logarithmic scale. The maximum errors amount to 0.28 μS and 0.022 μS for the measurement ranges of 0.1 μS to 10 mS and 0.01 μS to 1 mS, respectively. These errors could be due to the measurement error of the reference resistance: an error similar to that shown in figure 5 can be caused by an error of only 0.0025% in the value of the reference resistance.

5.3. The effect of the parasitic capacitance

The effects of the parasitic capacitor C_{sp} on the interface accuracy were measured for $C_F = 1$ nF, $R_{ref} = 1000.06 \ \Omega$ and $G_S = 49.986 \ \mu$S. The results are shown in figure 6. It is shown that up to $C_{sp} = 1$ nF the measurement error is less than 6 nS. When the measured conductance G_S is reduced to, for instance, 1 μS, the parasitic-capacitance effect on the standard deviation is similar to that shown in figure 6. However, in this case the measured error is reduced with a factor of 3. For low values of the parasitic capacitances good agreement is found between the measurement results depicted in figure 6 and those of figure 5.

5.4. The effect of the reference resistor

The effect of the reference resistor R_{ref} on the interface accuracy and resolution was measured with $G_S = 49.986$ μS and a measurement time of 160 ms (see figure 7). As expected, a larger reference resistance results in a lower standard deviation. However, the maximum measurable conductance is reduced (see figure 5).

6. Conclusions

In this paper, an interface for grounded conductivity sensors has been proposed and experimentally evaluated. A high accuracy has been achieved by applying ac square-wave excitation, chopping and auto-calibration. The controllable excitation signal for conductivity sensors enables us to avoid occurrence of electrolysis. The effects of the main non-idealities have been analyzed. The results of these analyses are very useful to optimize the interface system. Depending on the application, the measurement range can be optimized by selecting the reference conductance. Experimental results show that, with a measurement time of about 160 ms, the interface can measure conductance with a standard deviation of about 5.6 nS, and a systematic error of 22 nS for a range from 0.01 μS to 1 mS. The proposed interface is very suitable for implementation in low-cost CMOS technology.

Acknowledgments

References

[1] Xu B, Zhang P, Li X and Tao N 2004 Direct conductance measurement of single DNA molecules in aqueous solution *Nano Lett.* **4** 1105–8

[2] Robinson D A, Jones S B, Wraith J M, Or D and Friedman S P 2003 A review of advances in dielectric and electrical conductivity measurement in soils using time domain reflectometry *Vadose Zone J.* **2** 444–75

[3] Thornton Inc. 2000 *Product Guide for Process Measurement Instrumentation* (USA: Thornton Inc.)

[4] Fougere A J, Brown N L and Hohart E 1992 *Integrated CTD Oceanographic Data Collection Platform OCEANOLOGY 92 (Brighton, UK)*

[5] Amber Science Inc. 1999 *Model 4081 Conductivity Meter* (USA: Amber Science Inc.)

[6] Teass H A 1980 Linear ground conductivity measuring system *US Patent Appl. No*. 4181880

[7] Evans J T, Forgang S and Itskovich G B 1998 Downhole multiphase flow sensor *US Patent Appl. No*. 5736637

[8] Barben T R 1978 Four electrode conductivity sensor *US Patent Appl. No*. 641254

[9] Li X and Meijer G C M 2005 A low-cost and accurate interface for four-electrode conductivity sensors *IEEE Trans. Instrum. Meas.* **54** 2433–7

[10] van der Goes F and Meijer G C M 1997 A universal transducer interface for capacitive and resistive sensor elements *Analog Integr. Circuits Signal Process.* **14** 249–60

[11] Gasulla M, Li X and Meijer G C M 2005 The noise performance of a high-speed capacitive-sensor interface based on a relaxation oscillator and a fast counter *IEEE Trans. Instrum. Meas.* **54** 1934–40

[12] Toth F N, Meijer G C M and Kerkvliet H M M 1996 A very accurate measurement system for multielectrode capacitive sensors *IEEE Trans. Instrum. Meas.* **45** 531–5

[13] van der Goes F M L and Meijer G C M 1996 Sigma-delta versus oscillator-based converters in low-cost accurate sensor systems *Proc. IMTC96* vol 2 pp 1151–3